nature COMMUNICATIONS

ARTICLE

Received 5 Jan 2016 | Accepted 1 Mar 2016 | Published 1 Apr 2016

DOI: 10.1038/ncomms11204 OPEN

Coupled molybdenum carbide and reduced graphene oxide electrocatalysts for efficient hydrogen evolution

Ji-Sen Li[1,2,*], Yu Wang[1,*], Chun-Hui Liu[1], Shun-Li Li[1], Yu-Guang Wang[2], Long-Zhang Dong[1], Zhi-Hui Dai[1], Ya-Fei Li[1] & Ya-Qian Lan[1]

Electrochemical water splitting is one of the most economical and sustainable methods for large-scale hydrogen production. However, the development of low-cost and earth-abundant non-noble-metal catalysts for the hydrogen evolution reaction remains a challenge. Here we report a two-dimensional coupled hybrid of molybdenum carbide and reduced graphene oxide with a ternary polyoxometalate-polypyrrole/reduced graphene oxide nanocomposite as a precursor. The hybrid exhibits outstanding electrocatalytic activity for the hydrogen evolution reaction and excellent stability in acidic media, which is, to the best of our knowledge, the best among these reported non-noble-metal catalysts. Theoretical calculations on the basis of density functional theory reveal that the active sites for hydrogen evolution stem from the pyridinic nitrogens, as well as the carbon atoms, in the graphene. In a proof-of-concept trial, an electrocatalyst for hydrogen evolution is fabricated, which may open new avenues for the design of nanomaterials utilizing POMs/conducting polymer/reduced-graphene oxide nanocomposites.

[1] Jiangsu Key Laboratory of Biofunctional Materials, College of Chemistry and Materials Science, Nanjing Normal University, Nanjing 210023, China. [2] Key Laboratory of Inorganic Chemistry in Universities of Shandong, Department of Chemistry and Chemical Engineering, Jining University, Qufu, Shandong 273155, China. * These authors contributed equally to this work. Correspondence and requests for materials should be addressed to Z.-H.D. (email: daizhihuii@njnu.edu.cn) or to Y.-Q.L. (email: yqlan@njnu.edu.cn).

To address the energy crisis and ameliorate environmental contamination, researchers have devoted considerable attention to hydrogen as promising alternative to fossil fuels. Electrochemical water splitting to produce hydrogen, or the hydrogen evolution reaction (HER), is the most economical and sustainable method for large-scale hydrogen production. Achieving this goal requires inexpensive electrocatalysts with high efficiency for the HER[1,2]. Although the best electrocatalysts are Pt or Pt-based materials, their high cost and low abundance substantially hamper their large-scale utilization[3–5]. Thus, the development of low-cost and earth-abundant non-noble-metal catalysts to replace Pt is an important and urgently needed for practical applications.

Because of their Pt-like catalytic behaviours[6], Mo-based compounds, such as Mo_2C[7–10], MoN[11–13], MoS_2 (refs 14–17), and others[18–20] have attracted substantial interest as a new class of electrocatalysts. To further enhance the HER activity, Mo-based compounds have been anchored onto conductive supports, such as carbon nanosheets (NSs)[21–23] and carbon nanotubes (CNTs)[11,24,25], which not only prevent Mo-based compounds from aggregating but also increase the dispersion of active sites. Among these conductive supports, reduced graphene oxide (RGO), particularly nitrogen (N)-doped RGO, has garnered much attention because of its excellent electron transport properties and chemical stability[26,27]. Therefore, RGO-supported Mo-based compounds appear to be highly active and stable electrocatalysts[11,25,28–30]. However, carbonization at high-reaction temperature during synthesis procedures leads to the sintering and aggregation of Mo-based-compound nanoparticles (NPs), thus reducing their number of exposed active sites and their specific surface area[8,19]. In addition, due to its strong π-stacking and hydrophobic interactions, RGO NSs usually aggregate, which hinders their practical application[31,32]. Preventing the RGO from re-stacking and the Mo-based compound NPs from aggregating during the synthesis of a porous uniform thin layer RGO-supported Mo-based electrocatalysts is critical to enhancing their catalytic performance.

We developed a new approach to integrate polyoxometalates (POMs) and pyrrole (Py) on graphene substrates via a "one-pot" method to obtain ternary POMs–polypyrrole/RGO (POMs–PPy/RGO) nanohybrid sheets with a uniform distribution. As an important family of transition-metal oxide clusters with excellent redox features[33,34], POMs provided an essential oxidizing medium for the oxidative polymerization of Py[35], and the POMs finally were converted into "heteropoly blue"[36]. Heteropoly blue can be used as a highly localized reducing agent and can further react with graphene oxide (GO) to restore the original POMs. With the polymerization of the Py monomers, POMs were dispersed into the PPy framework. Meanwhile, RGO was homogeneously dispersed and segregated by both the POMs and PPy during the synthesis of POMs–PPy/RGO. Thus, RGO-supported Mo-based catalysts prepared with POMs–PPy/RGO as a precursor may efficiently hinder the Mo sources and graphene from aggregating during the process of forming the RGO-supported NPs. To the best of our knowledge, reports on POMs, PPy and RGO ternary hybrids by a green and one-pot redox relay reaction are rare. More importantly, the coupled hybrid with both Mo_2C and RGO has not been previously prepared with a ternary hybrid as the precursor.

In this work, we carefully design and fabricate a two-dimensional (2D) coupled hybrid consisting of Mo_2C encapsulated by N, phosphorus (P)-codoped carbon shells and N, P-codoped RGO (denoted as Mo_2C@NPC/NPRGO) using a PMo_{12} ($H_3PMo_{12}O_{40}$)–PPy/RGO nanocomposite as the precursor. Notably, the entire polymerization and the reductive reactions are triggered by PMo_{12} without any additional oxidants or reductants, leading to a synthetic process that is green, efficient and economical. PPy was used as both the carbon and nitrogen sources as well as the reducing agent for GO. Three main advantages of this method are attributed to the Mo_2C@NPC/NPRGO hybrid: (1) due to the unique structure of PMo_{12}–PPy/RGO, the Mo_2C NPs are nanosized and uniformly embedded in the carbon matrix without aggregation; (2) the Mo_2C NPs are coated with carbon shells, which effectively prevent Mo_2C NPs from aggregating or oxidizing and impart them with fast electron transfer ability; and (3) owing to the heteroatom dopants (N, P), a large number of active sites are exposed. Overall, taking advantage of the synergistic catalytic effects, the Mo_2C@NPC/NPRGO catalyst exhibits excellent electrocatalytic activity for the HER, with a low onset overpotential of 0 mV (vs reversible hydrogen electrode (RHE)), a small Tafel slope of 33.6 mV dec^{-1}, and excellent stability in acidic media. Its HER catalytic activity, which is comparable to that of commercial Pt–C catalyst, even superior to those of the best reported non-noble-metal catalysts. In addition, we further investigate the nature of catalytically active sites for the HER using density functional theory (DFT). This approach provides a perspective for designing 2D nanohybrids with transition-metal carbides and RGO as HER catalysts.

Results

Catalyst synthesis and characterization. Mo_2C@NPC/NPRGO was synthesized as follows: (1) the PMo_{12}–PPy/RGO nanocomposite was synthesized via a green one-pot redox relay reaction. The nanocomposite was then carbonized under a flow of ultrapure N_2 at 900 °C for 2 h at a heating rate of 5 °C min^{-1}. Finally, the obtained samples were acid etched in 0.5 M H_2SO_4 for 24 h with continuous agitation at 80 °C to remove unstable and inactive species. The etched samples were thoroughly washed with deionized water until the pH of the wash water was neutral (Fig. 1).

Figure 2a shows a scanning electron microscopy (SEM) image of PMo_{12}–PPy/RGO. The rough surfaces and wrinkled edges on the sheet-like structures were due to the intercalation and

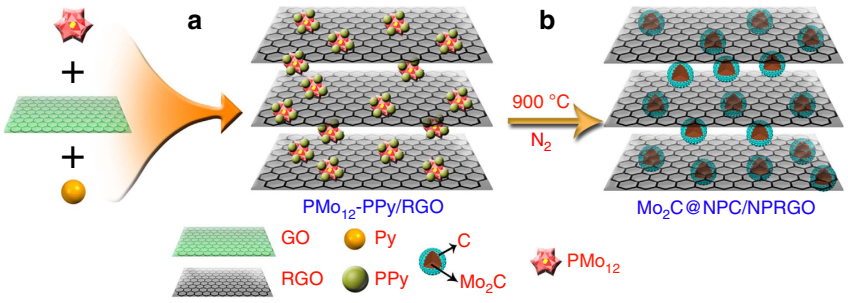

Figure 1 | Schematic illustration of the synthetic process of Mo_2C@NPC/NPRGO. (**a**) Synthesis of PMo_{12}–PPy/RGO via a green one-pot redox relay reaction. (**b**) Formation of Mo_2C@NPC/NPRGO after carbonizing at 900 °C.

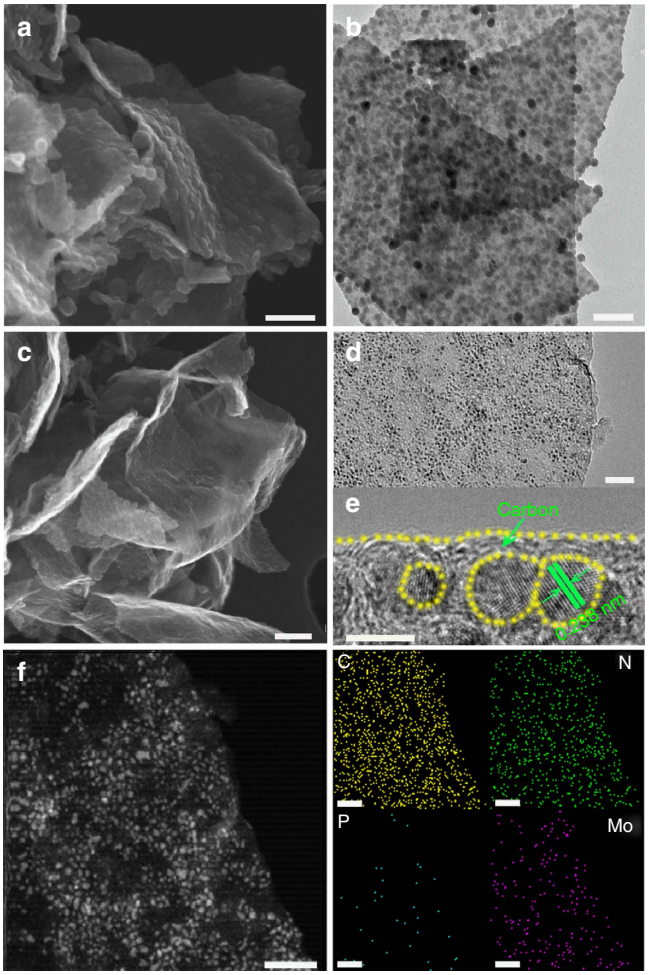

Figure 2 | Characterization of the PMo_{12}–PPy/RGO and Mo_2C@NPC/NPRGO hybrids. (**a**) SEM and (**b**) TEM images of PMo_{12}–PPy/RGO. (**c**) SEM, (**d**) TEM, (**e**) HRTEM and (**f**) STEM images and EDX elemental mapping of C, N, P and Mo of Mo_2C@NPC/NPRGO. Scale bar: **a**,**b**,**c** (200 nm); **d** (100 nm); **e** (5 nm) and **f** (50 nm).

polymerization of Py. A transmission electron microscopy (TEM) image of PMo_{12}–PPy/RGO revealed that a large amount of PPy/PMo_{12} NPs were homogeneously coated onto the RGO NSs and that voids were present (Fig. 2b). As evident in Fig. 2c and d, the morphologies of Mo_2C@NPC/NPRGO were similar to that of PMo_{12}–PPy/RGO after carbonization. The nanosized Mo_2C NPs with diameters of ~2–5 nm were uniformly decorated on the RGO sheets at a high density, which was attributed to the distinct porous structure of PMo_{12}–PPy/RGO. The high-resolution TEM (HRTEM) image exhibited clear lattice fringes with an interplanar distance of 0.238 nm, corresponding to the (111) planes of Mo_2C (Fig. 2e)[37]. Notably, the Mo_2C NPs were embedded in the carbon shells, which can efficiently prevent the aggregation and/or excessive growth of Mo_2C NPs[22]. Figure 2f shows the scanning TEM (STEM) and corresponding energy dispersive X-ray spectroscopy (EDX) elemental mapping images, which confirmed that C, Mo, N and P were distributed on the Mo_2C@NPC/NPRGO surface, consistent with the EDX spectrum (Supplementary Fig. 1). These results confirm the successful synthesis of the Mo_2C@NPC/NPRGO nanocomposite.

For comparison, the nanohybrid of Mo_2C encapsulated by N, P-codoped carbon (defined as Mo_2C@NPC) was also synthesized through a similar preparation procedure without GO. Supplementary Fig. 2a shows aggregation of PPy/PMo_{12} NPs. Supplementary Fig. 2b and c reveals that Mo_2C NPs tended to agglomerate during the heat treatment to form large NPs, which decreased the exposed active surface. Supplementary Fig. 2d demonstrates the STEM and EDX elemental mapping images of Mo_2C@NPC. These data verified that the Mo_2C@NPC material contained C, N, P and Mo elements, consistent with the EDX results (Supplementary Fig. 1b). Hence, these results sufficiently confirm that the presence of GO plays an important role in the generation of highly dispersed and nanosized Mo_2C NPs.

Supplementary Fig. 3 shows the powder X-ray diffraction patterns of Mo_2C@NPC and Mo_2C@NPC/NPRGO. The broad peak at ~25° was ascribed to carbon[38,39]. The other peaks located at 37.9, 43.7, 61.6 and 75.6° were indexed to the (111), (200), (220) and (311) planes of Mo_2C (JCPDS, No. 15-0457), respectively; these peaks were broad and exhibited low intensity because of the smaller crystallites of Mo_2C or Mo_2C coated with amorphous carbon[21,40,41]. Beside, the degrees of graphitization of the two catalysts were analyzed by Raman spectra (Supplementary Fig. 4). As is well-known, the ratio between the D (1,350 cm^{-1}) and G band (1,580 cm^{-1}) intensities (I_D/I_G) is an important criterion to judge the degree of the graphitization[9,28]. Compared to Mo_2C@NPC, the I_D/I_G of Mo_2C@NPC/NPRGO is higher, implying that more defects formed on the RGO sheets, thus favoring the accessibility of more active sites and enhancing the electrocatalytic performance. The Brunauer–Emmett–Teller (BET) surface areas of Mo_2C@NPC and Mo_2C@NPC/NPRGO calculated by the N_2 sorption isotherms were 55 and 190 $m^2 g^{-1}$, respectively (Supplementary Fig. 5a). Mo_2C@NPC showed a microporous structure, with pore sizes mainly in the range from 1 to 2 nm (Supplementary Fig. 5b), whereas the corresponding pore size distribution of Mo_2C@NPC/NPRGO was mainly concentrated in the range from 1 to 10 nm, which was characteristic of a microporous and mesoporous structure (Supplementary Fig. 5c). Overall, the large surface area and enriched porous structures efficiently facilitate electrolyte penetration and charge transfer[9].

X-ray photoelectron spectroscopy (XPS) analyses of Mo_2C@NPC/NPRGO catalysts were carried out to elucidate their valence states and compositions. As observed, the XPS spectrum of Mo_2C@NPC/NPRGO (Supplementary Fig. 6) indicated the presence of C, N, O, P and Mo in the catalyst. The deconvoluted C1*s* spectrum is shown in Fig. 3a, and the main peak at 284.6 eV implies that the graphite carbon is the majority species[22]. The deconvolution of N1*s* energy level signals for Mo_2C@NPC/NPRGO revealed the peaks at 398.6 and 401.3 eV, which were assigned to pyridinic and graphitic N (Fig. 3b), respectively[21,27]. From Fig. 3c, it can be seen that the P2*p* peaks at about 133.5, and 134.8 eV were attributed to P–C and P–O bonding, respectively[18,28]. Besides, the high-resolution Mo 3*d* XPS revealed that the peak at 228.8 eV was attributable to Mo^{2+}, stemming from Mo_2C. In parallel, as a consequence of surface oxidation, the peaks at 232.05 and 235.2 were attributable to MoO_3 and that at 232.7 eV was assignable to MoO_2 (refs 8,21); both of these species are inactive toward the HER (Fig. 3d). For comparison, Mo_2C@NPC is shown in Supplementary Fig. 7. All of these data were similar to those for Mo_2C@NPC/NPRGO. The corresponding atomic percentages of the different catalysts measured by XPS are listed in Supplementary Table 1.

Electrocatalytic HER performance. A three-electrode system was adopted to evaluate the electrocatalytic activities of Mo_2C@NPC/NPRGO toward the HER in 0.5 M H_2SO_4 at 100 mV s^{-1}. For comparison, Mo_2C@NPC and commercial Pt–C (20 wt% Pt on carbon black from Johnson Matthey) were also assessed. The corresponding polarization curves without IR compensation are shown in Fig. 4a. All potentials in this work are reported vs RHE. As expected, the commercial Pt–C displayed the highest

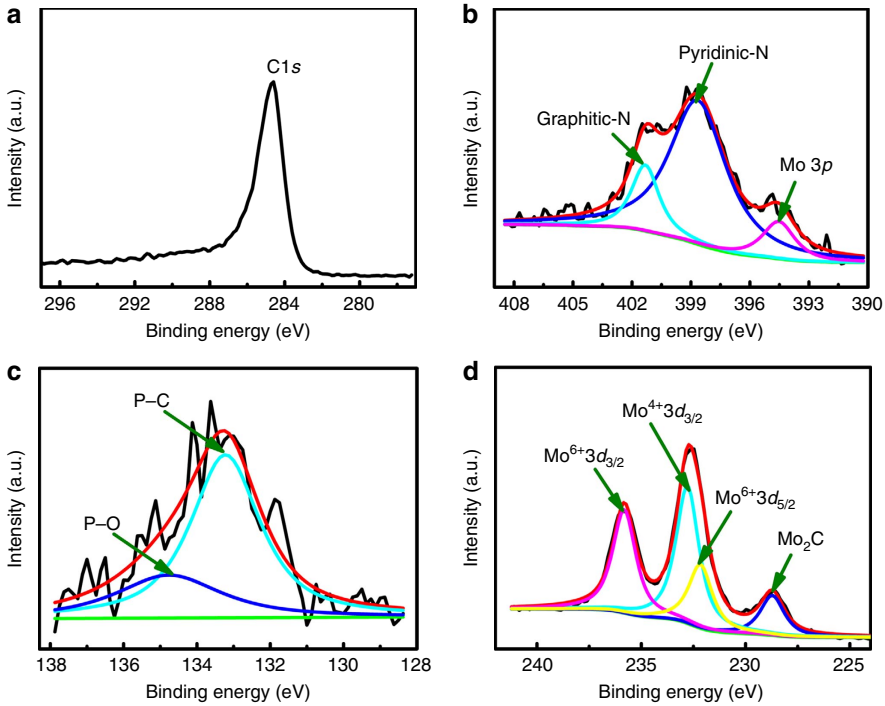

Figure 3 | Compositional characterization of the Mo_2C@NPC/NPRGO. XPS high-resolution scans of (**a**) C 1*s*, (**b**) N 1*s*, (**c**) P 2*p* and (**d**) Mo 3*d* electrons of Mo_2C@NPC/NPRGO.

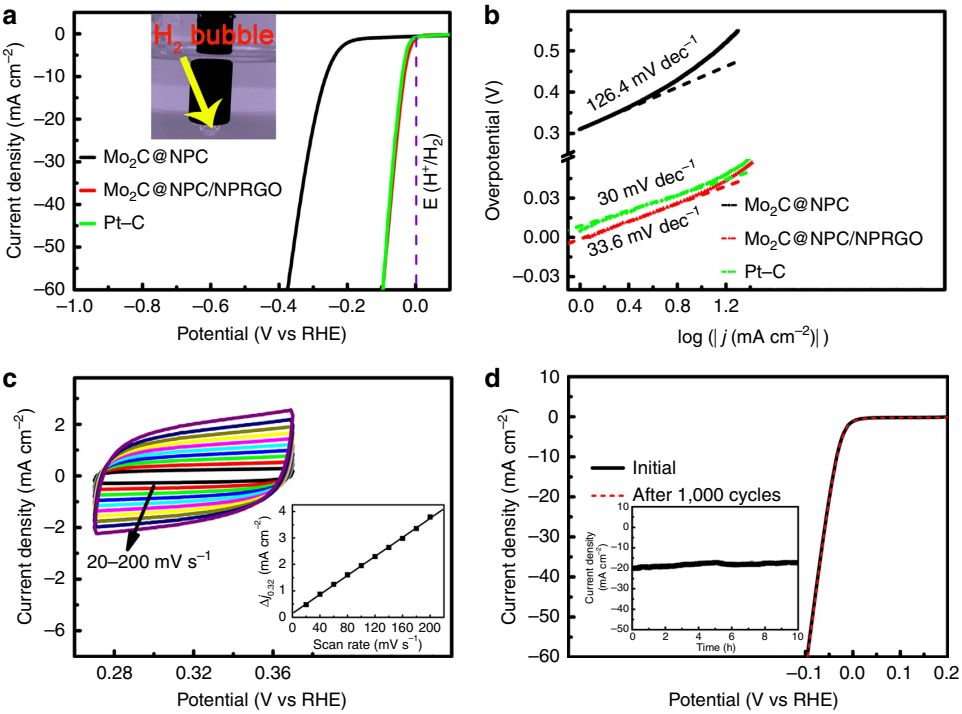

Figure 4 | HER activity characterization. (**a**,**b**) Polarization curves and Tafe plots of Mo_2C@NPC, Mo_2C@NPC/NPRGO and Pt-C. (inset: the production of H_2 bubbles on the surface of Mo_2C@NPC/NPRGO). (**c**) CVs of Mo_2C@NPC/NPRGO with different rates from 20 to 200 mV s^{-1}. Inset: The capacitive current at 0.32 V as a function of scan rate for Mo_2C@NPC/NPRGO. (**d**) Polarization curves of Mo_2C@NPC/NPRGO initially and after 1,000 CV cycles. Inset: Time-dependent current density curve of Mo_2C@NPC/NPRGO under a static overpotential of 48 mV for 10 h.

electrocatalytic activity, with an onset overpotential of nearly zero[30]. The Mo_2C@NPC catalyst exhibited far inferior HER activity. Impressively, Mo_2C@NPC/NPRGO exhibited the lowest onset overpotential of 0 mV, approaching the performance of commercial Pt–C. Moreover, it was clearly observed that the cathodic current rose sharply with more negative potentials. Generally, the potential value for a current density of 10 mA cm^{-2} is an important reference because solar-light-

Table 1 | Comparison of catalytic parameters of different HER catalysts.

Catalyst	Onset potential (mV vs RHE)	Overpotential at 10 mA cm^{-2} (mV vs RHE)	j_0 (mA cm^{-2})	Tafel slope (mV dec^{-1})
Mo_2C@NPC	137	260	3.16×10^{-3}	126.4
Mo_2C@NPC/NPRGO	0	34	1.09	33.6
Pt-C	0	40	0.39	30

HER, H_2 evolution reaction; Pt-C, 20 wt% Pt on carbon lack from Johnson-Matthey; RHE, reversible hydrogen electrode.
j_0 represents exchange current density that was calculated from Tafel curves using extrapolation method.

coupled HER apparatuses usually operate at 10–20 mA cm^{-2} under standard conditions (1 sun, AM 1.5)[4]. To achieve this current density, Mo_2C@NPC requires an overpotential of 260 mV. Strikingly, Mo_2C@NPC/NPRGO required only ~34 mV to achieve a 10 mA cm^{-2} current density, even superior to commercial Pt–C (40 mV) (Table 1). To the best of our knowledge, this overpotential is superior to those of all previously reported non-noble-metal electrocatalysts for the HER, such as $MoS_2/CoSe_2$ (ref. 15), MoO_2 (ref. 18), Mo_2C/CNT[24] and CoNi@NC[40] (Supplementary Table 2).

To elucidate the HER mechanism, Tafel Plots were fitted to Tafel equation (that is, $\eta = b \log(j) + a$, where b is the Tafel slope, and j is the current density), as shown Fig. 4b. The Tafel slope of commercial Pt–C was ~30 mV dec^{-1}, which was in agreement with the reported value, thus supporting the validity of our electrochemical measurements[30]. The Tafel slope of Mo_2C@NPC/NPRGO was 33.6 mV dec^{-1}, which indicated higher performance than that of Mo_2C@NPC (126.4 mV dec^{-1}). Meanwhile, the Tafel slope of Mo_2C@NPC/NPRGO suggested that hydrogen evolution on the Mo_2C@NPC/NPRGO electrode probably proceeds via a Volmer–Tafel mechanism, where the recombination is the rate-limiting step[17]. The exchange current density (j_0) was extrapolated from the Tafel plots. Notably, Mo_2C@NPC/NPRGO displayed the largest j_0 of 1.9×10^{-3} A cm^{-2}, which was nearly three times larger than the j_0 of Pt–C (0.39×10^{-3} A cm^{-2}) (Table 1) and was substantially greater than those of other recently reported non-noble-metal catalysts (Supplementary Table 2). This performance of Mo_2C@NPC/NPRGO demonstrates favourable HER kinetics at the Mo_2C@NPC/NPRGO/electrolyte interface.

The electrochemical double-layer capacitance (EDLC, C_{dll}) was measured to investigate the electrochemically active surface area. Cyclic voltammetry (CV) was performed in the region from 0.27 to 0.37 V at rates varying from 20 to 200 mV s^{-1} (Fig. 4c and Supplementary Fig. 8). The C_{dll} of Mo_2C@NPC/NPRGO (17.9 mF cm^{-2}) was ~195 times larger than that of Mo_2C@NPC (0.092 mF cm^{-2}). Thus, the large j_0 value of Mo_2C@NPC/NPRGO may benefit from both its large BET surface area and its large EDLC.

To gain further insight into the electrocatalytic activity of Mo_2C@NPC/NPRGO for the HER, we performed electrochemical impedance spectroscopy (EIS). The Nyquist plots of the EIS responses are shown in Supplementary Fig. 9. Compared with the Nyquist plot of Mo_2C@NPC, that of Mo_2C@NPC/NPRGO showed a much smaller semicircle, suggesting that Mo_2C@NPC/NPRGO has lower impedance. This result proves that the catalyst affords markedly faster HER kinetics due to the presence of the RGO support.

Long-term stability is also critical for HER catalysts. To probe the durability of the Mo_2C@NPC/NPRGO catalyst, continuous CV was performed between −0.2 and 0.2 V at a 100 mV s^{-1} scan rate in 0.5 M H_2SO_4 solution (Fig. 4d). As observed, the polarization curve for Mo_2C@NPC/NPRGO remained almost the same after 1,000 cycles. In addition, the durability of Mo_2C@NPC/NPRGO was also examined by electrolysis at a static overpotential of 48 mV. The inset of Fig. 4d shows that the current density experienced a negligible loss at ~20 mA cm^{-2} for 10 h. For comparison, the durability of the Mo_2C@NPC catalyst was examined by the same methods (Supplementary Fig. 10). This is reconfirming that Mo_2C@NPC and Mo_2C@NPC/NPRGO are stable electrocatalysts in acidic solutions.

In control experiments, we investigated the effect of the PMo_{12} content on electrocatalytic performance. Two other catalysts with different PMo_{12} contents (1.1 and 3.3 g) were synthesized (denoted as Mo_2C@NPC/NPRGO-1.1 and Mo_2C@NPC/NPRGO-3.3). The morphology, structure and composition of these two catalysts were studied by SEM, TEM, HRTEM, STEM, EDX, elemental mapping, powder X-ray diffraction patterns and XPS in detail (Supplementary Figs 11–16). The HER activities of Mo_2C@NPC/NPRGO-1.1 and -3.3 were also evaluated using the same measurements. As seen from Fig. 5a,b, Mo_2C@NPC/NPRGO showed the lowest onset overpotential and the smallest Tafel slope among the three samples. We speculate that these results are likely related to the amount and distribution of active sites. Because of the lower amount of Mo_2C NPs in Mo_2C@NPC/NPRGO-1.1, the corresponding electrocatalytic activity was poorer than that of Mo_2C@NPC/NPRGO. In contrast, a larger number of Mo_2C NPs in Mo_2C@NPC/NPRGO-3.3 aggregated together, which is also unfavourable for the HER. These results demonstrate that the amount of PMo_{12} substantially influences the HER performance.

We subsequently studied the influence of carbonization temperature under the given conditions. Supplementary Figs 17–22 show the morphology, structure and composition of the two samples carbonized at 700 and 1,100 °C (defined as PMo_{12}–PPy/RGO-700 and Mo_2C@NPC/NPRGO-1100), respectively. The onset overpotentials of PMo_{12}–PPy/RGO-700 and Mo_2C@NPC/NPRGO-1100 were 20 and 27 mV, respectively, and the Tafel slopes were 48.4 and 70.1 mV dec^{-1}, respectively (Fig. 5c and d). Among these catalysts, the Mo_2C@NPC/NPRGO catalyst exhibited the optimal HER activity, possibly because active sites of Mo_2C were not produced when PMo_{12}–PPy/RGO is carbonized at 700 °C; the high–carbonization temperature led to substantial sintering and aggregation of Mo_2C NPs, which further reduced the density of highly active sites. Meanwhile, the N content decreased with increasing carbonization temperature (Supplementary Table 1). All of these results were consistent with the SEM, TEM, XRD, thermogravimetric analysis and XPS results (Supplementary Figs 17–22). Therefore, in this work, the selection of the correct PMo_{12} content and carbonization temperature was critical to forming high-HER active sites.

Theoretical investigation. The aforementioned experimental results demonstrated that the Mo_2C@NPC/NPRGO composite exhibits excellent electrocatalytic activity toward the HER because of the synergistic effects of Mo_2C and NPC/NPRGO. To elucidate the mechanism underlying the superior HER activity of the Mo_2C@NPC/NPRGO composite, we performed a series of DFT calculations (Supplementary Fig. 23 and Supplementary Table 3). Theoretically, the HER pathway can be depicted as a three-state

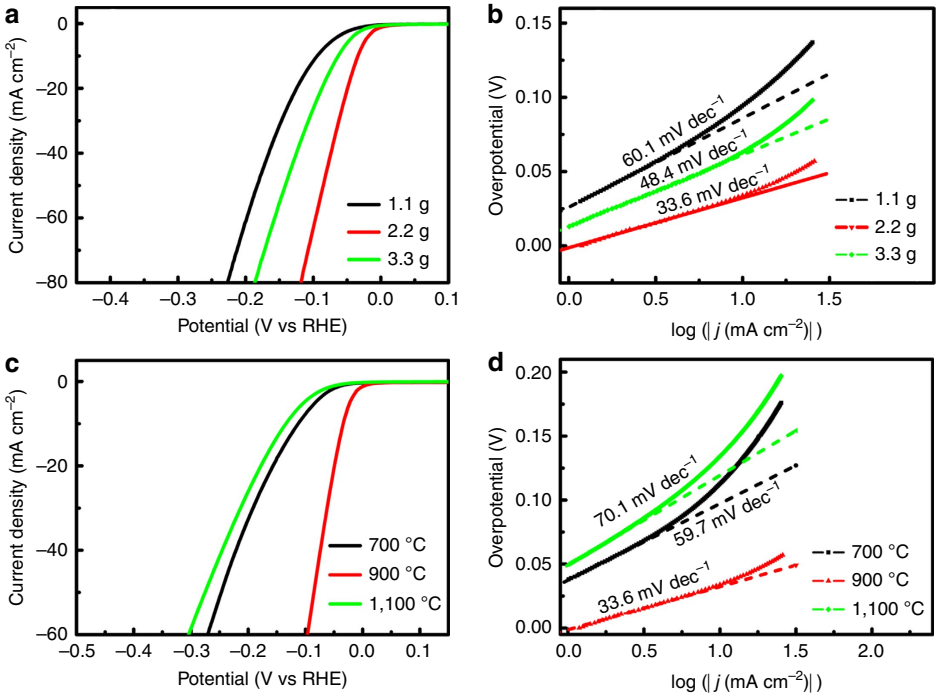

Figure 5 | Comparison of the HER performance of different electrocatalysts. (**a**,**b**) Polarization curves and Tafe plots of Mo_2C@NPC/NPRGO with different mass of PMo_{12} (1.1, 2.2 and 3.3 g). (**c**,**d**) Polarization curves and Tafe plots of Mo_2C@NPC/NPRGO (2.2 g) at different carbonization temperature.

diagram containing an initial state of $H^+ + e^-$, an intermediate state of adsorbed H (H*, where * denotes an adsorption site), and a final state of 1/2 the H_2 product[5,22]. Generally, a good hydrogen evolution catalyst should have a free energy of adsorbed H of approximately zero ($\Delta G_{H^*} \approx 0$), which can provide a fast proton/electron-transfer step as well as a fast hydrogen release process[42]. Because only trace amounts of P were present in the Mo_2C@NPC/NPRGO hybrid compared to the N content, we investigated only the effect of N doping (graphitic N and pyridinic N) on the catalytic effect of the hybrids. Figure 6 shows the calculated free energy diagram for the HER in various studied systems.

According to our computational results, pristine graphene had an endothermic ΔG_{H^*} of 1.82 eV, implying an energetically unfavourable interaction with hydrogen. Therefore, the HER can barely proceed on pristine graphene because of the slow proton/electron transfer. On the other hand, the (001) surface of Mo_2C had a strong interaction with H, as indicated by the exothermic ΔG_{H^*} of -0.82 eV, which would subsequently lead to poor HER performance because of the foreseeable difficulty of hydrogen release. Moreover, N-doped graphene exhibited low catalytic activity toward the HER. Specifically, the ΔG_{H^*} values for graphitic-N- and pyridinic-N-doped graphene were 0.89 and -2.04 eV, respectively.

However, the catalytic activity of graphene and N-doped graphene were substantially improved when they were anchored to the surface of Mo_2C. For example, the ΔG_{H^*} values for Mo_2C@C and Mo_2C@C-graphitic N were 0.41 and 0.69 eV, respectively, which were much lower than those of suspended graphene (1.82 eV) and N-doped graphene (0.89 eV). The ΔG_{H^*} of Mo_2C@C (0.41 eV) indicated that the graphene C atoms in the hybrid also play an important role in the HER activity. In particular, due to the synergistic effect between Mo_2C and C-pyridinic N, Mo_2C@C-pyridinic N had a favourable ΔG_{H^*} (-0.22 eV) for the adsorption and desorption of hydrogen. Therefore, the active sites for the HER should be composed mainly of pyridinic N atoms and C atoms of graphene rather than

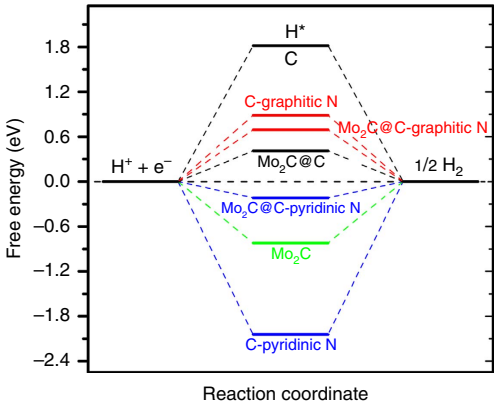

Figure 6 | DFT-calculated HER activities. Calculated free energy diagram for HER on various studied system.

graphitic N atoms. We note here that, according to the results of XPS analysis, the major type of N in Mo_2C@NPC/NPRGO was pyridinic N, which means that Mo_2C@NPC/NPRGO would manifest a high density of active sites and would consequently present a high-current density at a low overpotential for the HER. Overall, the experimental and theoretical results verified that as-synthesized Mo_2C@NPC/NPRGO is an unexpected and highly efficient HER electrocatalyst.

Discussion

In view of the aforementioned considerations, the amazing HER activities of the Mo_2C@NPC/NPRGO are postulated to originate from the following reasons: (1) the small size of Mo_2C NPs favors the exposure of an abundance of available active sites, which may enhance the catalytic activity for the HER[7,21,28]; (2) the introduction of heteroatoms (N, P) into the carbon

structure results in charge density distribution and asymmetry spin, thus enhancing the interaction with H^+ (refs 18,27). Especially, pyridinic N is favourable for highly efficient catalytic performance[43,44]; (3) as an advanced support, RGO can increase the dispersion of PMo_{12} to further obtain highly dispersed Mo_2C during the carbonization process. Meanwhile, the outstanding electrical conductivity of RGO facilitates charge transfer in the catalyst[11,25]; (4) the robust conjugation between Mo_2C and NPC/NPRGO provides a resistance-less path favourable for fast electron transfer. The carbon shells may hamper the aggregation of Mo_2C NPs[21] and promote electron penetration from Mo_2C to RGO[22]. Furthermore, the geometric confinement of Mo_2C inside the carbon shells can also enhance the catalytic activity for the HER[40] and (5) the unique structure of Mo_2C@NPC/NPRGO is favourable for the fast mass transport of reactants and facilitates electron transfer[26,39]. Because of the synergistic catalytic effects of the aforementioned factors, the Mo_2C@NPC/NPRGO catalyst exhibits potent HER activity.

In summary, we designed and developed a novel architecture that is composed of Mo_2C NPs, NPC and NPRGO by simply carbonizing a ternary PMo_{12}–PPy/RGO nanocomposite. The effect of the PMo_{12} content and carbonization temperature on the HER activity was investigated in detail. The RGO-supported Mo-based catalysts prepared with PMo_{12}–PPy/RGO as the precursor may efficiently hinder Mo sources and graphene from aggregating during the formation of RGO-supported Mo_2C NPs. The obtained Mo_2C@NPC/NPRGO nanocomposite exhibits the best HER performance and high stability as an electrocatalyst in an acidic electrolyte reported to date. Theoretical studies demonstrated that the synergistic effect between Mo_2C and C-pyridinic N contributes to the excellent HER activity of the Mo_2C@NPC/NPRGO nanocomposite, in accordance with the experimental results. This proof-of-concept study not only offers novel hydrogen-evolving electrocatalysts with excellent activity but also opens new avenues for the development of other 2D coupled nanohybrids with transition-metal carbides and RGO using POMs/conducting polymer/RGO as a precursor. These catalysts can also be explored as highly efficient electrocatalysts for oxygen reduction reaction (ORR), HER and lithium batteries.

Methods

Synthesis of PMo_{12}–PPy/RGO and Mo_2C@NPC/NPRGO hybrids. In a typical synthesis, GO NSs were pre-synthesized by chemical oxidation exfoliation of natural graphite flakes using a modified Hummers method[45]. The obtained GO NSs were dispersed in de-ionized water by ultrasonication to form a suspension with the concentration of 1 mg ml^{-1}. Around 12.5 ml of such GO suspension and 150 ml of 2 mM PMo_{12} solution were added into a clean three-necked flask, respectively, and mixed uniformly under a strong ultrasonication bath. Subsequently, Py monomer solution by dispersing 230 μl of Py in 15 ml de-ionized water, was slowly dropped into the above mixed PMo_{12}/GO suspension. With the addition of Py monomer solution, the reaction system gradually turned from yellow-brown to deep blue and a black precipitate began to generate after about 5 min. Finally, the reactor was transferred to an oil bath and allowed to react for 30 h at 50 °C under vigorously magnetic stirring. After separated by centrifugation and washed with deionized water and anhydrous ethanol for several times, the black PMo_{12}–PPy/RGO ternary nanohybrids were obtained, which were dried in vacuum at 50 °C. In control experiments, PMo_{12}–PPy/RGO (1.1) and PMo_{12}–PPy/RGO (3.3) were synthesized by identical condition except that the amount of PMo_{12} is 1.1 and 3.3 g, respectively.

To prepare the Mo_2C@NPC/NPRGO nanocomposite, 2 g of PMo_{12}–PPy/RGO was carbonized in a flow of ultrapure N_2 at 900 °C for 2 h with the heating rate of 5 °C min^{-1}. The obtained samples were acid etched in H_2SO_4 (0.5 M) for 24 h with continuous agitation at 80 °C to remove unstable and inactive species. The etched samples were then thoroughly washed with de-ionized water until reaching a neutral pH, and defined as Mo_2C@NPC/NPRGO, Mo_2C@NPC/NPRGO-1.1 and -3.3, respectively.

Synthesis of PMo_{12}–PPy and Mo_2C@NPC composites. The synthetic procedure is very similar to PMo_{12}–PPy/RGO without GO. Likewise, the preparation of Mo_2C@NPC composite is identical with that of Mo_2C@NPC/NPRGO.

Characterization. The TEM and HRTEM images were recorded on JEOL-2100F apparatus at an accelerating voltage of 200 kV. Surface morphologies of the carbon materials were examined by a SEM (JSM-7600F) at an acceleration voltage of 10 kV. The EDX was taken on JSM-5160LV-Vantage-typed energy spectrometer. The XRD patterns were recorded on a D/max 2500VL/PC diffractometer (Japan) equipped with graphite monochromatized Cu Kα radiation ($\lambda = 1.54060$ Å). Corresponding work voltage and current is 40 kV and 100 mA, respectively. XPS was recorded by a scanning X-ray microprobe (PHI 5000 Verasa, ULAC-PHI, Inc.) using Al Kα radiation and the C1*s* peak at 284.8 eV as internal standard. The Raman spectra of dried samples were obtained on Lab-RAM HR800 with excitation by an argon ion laser (514.5 nm). The nitrogen adsorption–desorption experiments were operated at 77 K on a Micromeritics ASAP 2050 system. BET surface areas were determined over a relative pressure range of 0.05–0.3, during which the BET plot is linear. The pore size distributions were measured by using the nonlocalized density functional theory method. Before the measurement, the samples were degassed at 150 °C for 10 h.

Electrochemical measurements. All electrochemical experiments were conducted on a CHI 760D electrochemical station (Shanghai Chenhua Co., China) in a standard three electrode cell in 0.5 M H_2SO_4 at room temperature. A glassy carbon electrode (3 mm in diameter), an Ag/AgCl with saturated KCl, and a Pt wire were used as the working electrode, reference and counter electrode, respectively. A total of 4 mg of the catalysts were dispersed in 2 ml of 9:1 v/v water/Nafion by sonication to form a homogeneous ink. Typically, 5 μl well-dispersed catalysts were covered on the glassy carbon electrode and then dried in an ambient environment for measurements. The electrocatalyst was prepared with a catalyst loading of 0.14 mg cm^{-2}. Commercial 20% Pt–C catalyst was also used as a reference sample. Linear sweep voltammetry was tested with a scan rate of 5 mV s^{-1}. EIS measurements were carried out from 1,000 kHz to 100 mHz with an amplitude of 10 mV at the open-circuit voltage. The electrochemical stability of the catalyst was conducted by cycling the potential between −0.3 and 0.3 V vs RHE at a scan rate of 100 mV s^{-1}. The Chronoamperometry were tested at an overpotential of −0.12 V vs RHE after equilibrium. To estimate the electrochemical active surface areas of the catalysts, CV was tested by measuring EDLC under the potential window of 0.19–0.39 vs RHE with various scan rate (20, 40, 60, 80, 100, 120, 140, 160, 180 and 200 mV s^{-1}). A flow of N_2 was maintained over the electrolyte during the experiment to eliminate dissolved oxygen. The potential vs RHE was converted to RHE via the Nernst equation: $E_{RHE} = E_{Ag/AgCl} + 0.059pH + E^{\theta}_{Ag/AgCl}$. In 0.5 M H_2SO_4, $E_{RHE} = 0.21\ V + E_{Ag/AgCl}$.

Computational details. DFT calculations were performed using the plane-wave technique implemented in the Vienna *ab initio* Simulation package[46]. The ion–electron interaction was treated within the projector-augmented plane wave pseudopotentials[47,48]. The generalized gradient approximation expressed by Perdew − Burke − Ernzerhof functional[49] and a plane-wave cutoff energy of 360 eV were used in all computations. The electronic structure calculations were employed with a Fermi-level smearing of 0.1 eV for all surface calculations and 0.01 eV for all gas-phase species. The Brillouin zone was sampled with $3 \times 3 \times 1$ *k*-points. The convergence of energy and forces were set to 1×10^{-5} eV and 0.02 eV Å^{-1}, respectively. A vacuum region of around 12 Å was set along the *z* direction to avoid the interaction between periodic images. More computational details are provided in Supplementary Note 1.

References

1. Turner, J. A. Sustainable hydrogen production. *Science* **305,** 972–974 (2004).
2. Wang, J. *et al.* Recent progress in cobalt-based heterogeneous catalysts for electrochemical water splitting. *Adv. Mater.* **28,** 215–230 (2016).
3. Stamenkovic, V. R. *et al.* Trends in electrocatalysis on extended and nanoscale Pt-bimetallic alloy surfaces. *Nat. Mater.* **6,** 241–247 (2007).
4. Walter, M. G. *et al.* Solar water splitting cells. *Chem. Rev.* **110,** 6446–6473 (2010).
5. Zheng, Y. *et al.* Hydrogen evolution by a metal-free electrocatalyst. *Nat. Commun.* **5,** 3783 (2014).
6. Levy, R. B. & Boudart, M. Platinum-like behavior of tungsten carbide in surface catalysis. *Science* **181,** 547–549 (1973).
7. Wu, H. B., Xia, B. Y., Yu, L., Yu, X. Y. & Lou, X. W. Porous molybdenum carbide nano-octahedrons synthesized via confined carburization in metal-organic frameworks for efficient hydrogen production. *Nat. Commun.* **6,** 6512 (2015).
8. Zhao, Y., Kamiya, K., Hashimoto, K. & Nakanishi, S. *In situ* CO_2-emission assisted synthesis of molybdenum carbonitride nanomaterial as hydrogen evolution electrocatalyst. *J. Am. Chem. Soc.* **137,** 110–113 (2015).
9. Ma, F. X., Wu, H. B., Xia, B. Y., Xu, C.Y. & Lou, X. W. Hierarchical β-Mo_2C nanotubes organized by ultrathin nanosheets as a highly efficient electrocatalyst for hydrogen production. *Angew. Chem. Int. Ed.* **54,** 15395–15399 (2015).
10. Liao, L. *et al.* A nanoporous molybdenum carbide nanowire as an electrocatalyst for hydrogen evolution reaction. *Energy Environ. Sci.* **7,** 387–392 (2014).

11. Youn, D. H. *et al.* Highly active and stable hydrogen evolution electrocatalysts based on molybdenum compounds on carbon nanotube–graphene hybrid support. *ACS Nano* **8,** 5164–5173 (2014).
12. Chen, W. F. *et al.* Biomass-derived electrocatalytic composites for hydrogen evolution. *Energy Environ. Sci.* **6,** 1818–1826 (2013).
13. Ma, L., Ting, L. R. L., Molinari, V., Giordano, C. & Yeo, B. S. Efficient hydrogen evolution reaction catalyzed by molybdenum carbide and molybdenum nitride nanocatalysts synthesized via the urea glass route. *J. Mater. Chem. A* **3,** 8361–8368 (2015).
14. Wang, H. *et al.* Transition-metal doped edge sites in vertically aligned MoS_2 catalysts for enhanced hydrogen evolution. *Nano Res.* **8,** 566–575 (2015).
15. Gao, M. R. *et al.* An efficient molybdenum disulfide/cobalt diselenide hybrid catalyst for electrochemical hydrogen generation. *Nat. Commun.* **6,** 5982 (2015).
16. Merki, D. & Hu, X. Recent developments of molybdenum and tungsten sulfides as hydrogen evolution catalysts. *Energy Environ. Sci.* **4,** 3878–3888 (2011).
17. Jaramillo, T. F. *et al.* Identification of active edge sites for electrochemical H_2 evolution from MoS_2 nanocatalysts. *Science* **317,** 100–102 (2007).
18. Tang, Y. J. *et al.* Porous molybdenum-based hybrid catalysts for highly efficient hydrogen evolution. *Angew. Chem. Int. Ed.* **54,** 12928–12932 (2015).
19. Vrubel, H. & Hu, X. Molybdenum boride and carbide catalyze hydrogen evolution in both acidic and basic solutions. *Angew. Chem. Int. Ed.* **51,** 12703–12706 (2012).
20. Faber, M. S. & Jin, S. Earth-abundant inorganic electrocatalysts and their nanostructures for energy conversion applications. *Energy Environ. Sci.* **7,** 3519–3542 (2014).
21. Ma, R. *et al.* Ultrafine molybdenum carbide nanoparticles composited with carbon as a highly active hydrogen-evolution electrocatalyst. *Angew. Chem. Int. Ed.* **54,** 14723–14727 (2015).
22. Liu, Y. *et al.* Coupling Mo_2C with nitrogen-rich nanocarbon leads to efficient hydrogen-evolution electrocatalytic sites. *Angew. Chem. Int. Ed.* **54,** 10752–10757 (2015).
23. Cui, W. *et al.* Mo_2C nanoparticles decorated graphitic carbon sheets: biopolymer-derived solid-state synthesis and application as an efficient electrocatalyst for hydrogen generation. *ACS Catal.* **4,** 2658–2661 (2014).
24. Chen, W. F. *et al.* Highly active and durable nanostructured molybdenum carbide electrocatalysts for hydrogen production. *Energy Environ. Sci.* **6,** 943–951 (2013).
25. Seol, M. *et al.* Mo-compound/CNT-graphene composites as efficient catalytic electrodes for quantum-dot-sensitized solar cells. *Adv. Energy Mater.* **4,** 1300775 (2014).
26. Duan, J., Chen, S., Chambers, B. A., Andersson, G. G. & Qiao, S. Z. 3D WS_2 nanolayers@heteroatom-doped graphene films as hydrogen evolution catalyst electrodes. *Adv. Mater.* **27,** 4234–4241 (2015).
27. Duan, J., Chen, S., Jaroniec, M. & Qiao, S. Z. Porous C_3N_4 nanolayers@N-graphene films as catalyst electrodes for highly efficient hydrogen evolution. *ACS Nano* **9,** 931–940 (2015).
28. Yan, H. *et al.* Phosphorus-modified tungsten nitride/reduced graphene oxide as a high-performance, non-noble-metal electrocatalyst for the hydrogen evolution reaction. *Angew. Chem. Int. Ed.* **54,** 6325–6329 (2015).
29. He, C. & Tao, J. Synthesis of nanostructured clean surface molybdenum carbides on graphene sheets as efficient and stable hydrogen evolution reaction catalysts. *Chem. Commun.* **51,** 8323–8325 (2015).
30. Li, Y. *et al.* MoS_2 nanoparticles grown on graphene: an advanced catalyst for the hydrogen evolution reaction. *J. Am. Chem. Soc.* **133,** 7296–7299 (2011).
31. Kamat, P. V. Graphene-based nanoarchitectures. anchoring semiconductor and metal nanoparticles on a two-dimensional carbon support. *J. Phys. Chem. Lett.* **1,** 520–527 (2009).
32. Huang, C., Li, C. & Shi, G. Graphene based catalysts. *Energy Environ. Sci.* **5,** 8848–8868 (2012).
33. Du, D. Y., Qin, J. S., Li, S. L., Su, Z. M. & Lan, Y. Q. Recent advances in porous polyoxometalate-based metal-organic framework materials. *Chem. Soc. Rev.* **43,** 4615–4632 (2014).
34. Cronin, L. & Müller, A. From serendipity to design of polyoxometalates at the nanoscale, aesthetic beauty and applications. *Chem. Soc. Rev.* **41,** 7333–7334 (2012).
35. Wang, T. *et al.* Electrochemically fabricated polypyrrole and MoS_x copolymer films as a highly active hydrogen evolution electrocatalyst. *Adv. Mater.* **26,** 3761–3766 (2014).
36. Zhou, D. & Han, B. H. Graphene-based nanoporous materials assembled by mediation of polyoxometalate nanoparticles. *Adv. Funct. Mater.* **20,** 2717–2722 (2010).
37. Ma, R., Hao, W., Ma, X., Tian, Y. & Li, Y. Catalytic ethanolysis of kraft lignin into high-value small-molecular chemicals over a nanostructured α-molybdenum carbide catalyst. *Angew. Chem. Int. Ed.* **53,** 7310–7315 (2014).
38. Zhou, W. *et al.* N-doped carbon-wrapped cobalt nanoparticles on *N*-doped graphene nanosheets for high-efficiency hydrogen production. *Chem. Mater.* **27,** 2026–2032 (2015).
39. Wu, R., Zhang, J., Shi, Y., Liu, D. & Zhang, B. Metallic WO_2–carbon mesoporous nanowires as highly efficient electrocatalysts for hydrogen evolution reaction. *J. Am. Chem. Soc.* **137,** 6983–6986 (2015).
40. Deng, J., Ren, P., Deng, D. & Bao, X. Enhanced electron penetration through an ultrathin graphene layer for highly efficient catalysis of the hydrogen evolution reaction. *Angew. Chem. Int. Ed.* **54,** 2100–2104 (2015).
41. Zheng, W. *et al.* Experimental and theoretical investigation of molybdenum carbide and nitride as catalysts for ammonia decomposition. *J. Am. Chem. Soc.* **135,** 3458–3464 (2013).
42. Hinnemann, B. *et al.* Biomimetic hydrogen evolution: MoS_2 nanoparticles as catalyst for hydrogen evolution. *J. Am. Chem. Soc.* **127,** 5308–5309 (2005).
43. Lai, L. *et al.* Exploration of the active center structure of nitrogen-doped graphene-based catalysts for oxygen reduction reaction. *Energy Environ. Sci.* **5,** 7936–7942 (2012).
44. Rao, C. V., Cabrera, C. R. & Ishikawa, Y. In search of the active site in nitrogen-doped carbon nanotube electrodes for the oxygen reduction reaction. *J. Phys. Chem. Lett.* **1,** 2622–2627 (2010).
45. Lee, J. H. *et al.* Restacking-inhibited 3D reduced graphene oxide for high performance supercapacitor electrodes. *ACS Nano* **7,** 9366–9374 (2013).
46. Kresse, G. & Hafner, J. *Ab initio* molecular dynamics for liquid metals. *Phys. Rev. B* **47,** 558–561 (1993).
47. Blöchl, P. E. Projector augmented-wave method. *Phys. Rev. B* **50,** 17953–17979 (1994).
48. Kresse, G. & Joubert, D. From ultrasoft pseudopotentials to the projector augmented-wave method. *Phys. Rev. B* **59,** 1758–1775 (1999).
49. Perdew, J. P., Burke, K. & Ernzerhof, M. Generalized gradient approximation made simple. *Phys. Rev. Lett.* **77,** 3865–3868 (1996).

Acknowledgements

This work was financially supported by the National Natural Science Foundation of China (No. 21371099, 21522305 and 21471080), the NSF of Jiangsu Province of China (No. BK20130043 and BK20141445), the Natural Science Foundation of Shandong Province (No. ZR2014BQ037), the Youths Science Foundation of Jining University (No. 2014QNKJ08), the Priority Academic Program Development of Jiangsu Higher Education Institutions and the Foundation of Jiangsu Collaborative Innovation Center of Biomedical Functional Materials.

Author contributions

Y.-Q.L. and J.-S.L. conceived the idea. J.-S.L., C.-H.L., Y.-G.W. and L.-Z.D. designed the experiments, collected and analysed the data. Y.-F.L. and Y.W. performed the DFT calculations. S.-L.L. and. Z.-H.D. assisted with the experiments and characterizations. J.-S.L. and Y.-Q.L. co-wrote the manuscript. All authors discussed the results and commented on the manuscript.

Additional information

Supplementary Information accompanies this paper at http://www.nature.com/naturecommunications

Competing financial interests: The authors declare no competing financial interests.

Reprints and permission information is available online at http://npg.nature.com/reprintsandpermissions/

How to cite this article: Li, J.-S. *et al.* Coupled Molybdenum Carbide and Reduced Graphene Oxide Electrocatalysts for Efficient Hydrogen Evolution. *Nat. Commun.* 7:11204 doi: 10.1038/ncomms11204 (2016).